



Activation of self-assembled CaWO₄ nanocrystals via Mn-incorporation toward nonenzymatic electrocatalytic glucose oxidation

Title	Activation of self-assembled CaWO ₄ nanocrystals via Mn-incorporation toward nonenzymatic electrocatalytic glucose oxidation
Author(s)	Nagy, Levente Alex;Besic, Hanka;Albero, Josep;Martínez-Belmonte, Marta;Soliman Tamayo, Borja Khatabi;Tong, Wenming;Farràs, Pau
Publication Date	2025-12-28
Publisher	American Chemical Society
Repository DOI	https://doi.org/10.1021/acsnm.5c04672

Activation of Self-Assembled CaWO_4 Nanocrystals via Mn-incorporation towards Nonenzymatic Electrocatalytic Glucose Oxidation

*Levente A. Nagy,[†] Hanka Besic,[†] Josep Albero,[‡] Marta Martínez-Belmonte,[§] Borja Khatabi
Soliman Tamayo,[†] Wenming Tong,^{†*} Pau Farràs^{†*}*

[†]School of Biological and Chemical Sciences, Ryan Institute, University of Galway, University
Road, Galway, H91 CF50, Ireland

[‡]Instituto Universitario de Tecnología Química, (CSIC-UPV), Universitat Politècnica de
València, Valencia 46022, Spain

[§]Institute of Chemical Research of Catalonia (ICIQ-CERCA), The Barcelona Institute of
Science and Technology (BIST), Avda. Països Catalans, 16, Tarragona, 43007, Spain

*Corresponding authors:
pau.farras@universityofgalway.ie
wenming.tong@universityofgalway.ie

Keywords: Calcium Tungstate, Mn-incorporation, Surface non-stoichiometry, Non-
enzymatic, Glucose electrooxidation

Abstract

Integrating foreign metal ions into mixed metal oxide scaffolds, such as CaWO_4 , by a wet
chemistry co-precipitation method is an efficient approach for regulating the chemical

composition, which determines the structure and properties and, in turn, offers a versatile platform for enhancements of intrinsic properties and introduction of additional attributes in the host material. In this work, a series of $\text{Ca}_{1-x}\text{Mn}_x\text{WO}_4$ was prepared via a co-precipitation process at 30 °C to exhibit sphere-like hierarchical structures assembled from individual nanocrystals. The solid solubility limit of Mn in CaWO_4 is estimated to be ~24% for this synthetic approach. The nanocrystals exhibit nonstoichiometric amorphous layers on the surface, which are expected for this type of materials synthesised under such a mild condition. The successful incorporation of Mn into the crystal lattice of CaWO_4 led to an isotropic contraction of the crystal unit cells, as well as the shifting and merging of several vibrational modes. Cyclic voltammetry confirmed the activity of $\text{Ca}_{1-x}\text{Mn}_x\text{WO}_4$ for electrooxidation of glucose, which is directly linked to the presence of Mn in CaWO_4 . With the highest Mn content, $\text{Ca}_{0.759}\text{Mn}_{0.241}\text{WO}_4$ achieved sensitivities of 3.81 and 0.99 $\mu\text{A}\cdot\text{mM}^{-1}\cdot\text{cm}^{-2}$ for glucose concentrations in the ranges of 0.002 – 0.2 and 0.2 – 1 mM respectively, which are 237 and 60 times increases from that of CaWO_4 . The limit of detection and lower limit of quantitation were estimated to be 14 and 48 μM , respectively, with reasonable reproducibility and repeatability.

Introduction

Foreign metal ions are widely utilised as additives to precursors in wet chemistry syntheses of metal and metal oxide nanomaterials for regulating their shapes, sizes, crystal structures, and chemical compositions,¹⁻⁴ which, in turn, modulate the physical and chemical properties.^{5,6} Chemical composition is often one of the key factors that determine the structure and properties of mixed metal oxides.⁷ In particular, nanomaterials prepared via wet chemistry approach under a mild condition could be described as having a core-shell structure in terms of their chemical compositions.⁸ The core is a stoichiometric compound as indicated by the corresponding chemical formula while the shell could be seen as a combined layer of a few sub-layers that

could include a surface crystalline layer that is slightly distorted, a nonstoichiometric surface layer, and/or a decorative layer with surface metal ions, hydration layers, and/or organic species from capping agents such as surfactants, polymer, or small organic molecules.⁹⁻¹¹ Since a high surface-to-volume ratio is a hallmark of nanomaterials, such a surface nonstoichiometry is fundamental to catalytic processes.

Mixed metal oxides are a broad class of important materials due to their applications in photonics,¹² electronics,¹³ electrochemistry,¹⁴ magnetics,¹⁵ and sensing¹⁶. Interestingly, due to the suitable material stability and facile preparation process (quick formation of crystalline nanoparticles at low temperature via simple co-precipitation process), mixed metal oxides, such as calcium tungstate (CaWO_4), are commonly chosen as substrates to design and develop materials for photoluminescence, optical thermometry, sensing, and catalysis.^{7,17,18} CaWO_4 is a prototype scheelite compound that has a close structural resemblance to many ABO_4 type materials including BaWO_4 , CaMoO_4 , and SrWO_4 . CaWO_4 was shown to be an ideal host for photoluminescent materials as demonstrated by core/shell structured multicolour phosphors via co-doping Na^+ and Ln^{3+} ($\text{Ln} = \text{Eu}, \text{Sm}, \text{Tb}, \text{and Dy}$) with efficient energy transfers from host to dopant at high doping levels ($>10\%$).¹⁹ At a low doping level, both $\text{CaWO}_4:\text{Eu}^{3+}$ (0.1%) and $\text{CaWO}_4:\text{Sm}^{3+}$ (0.5%) exhibited strong performances for multimode optical thermometry with broad temperature ranges and high sensitivities.²⁰

Moreover, CaWO_4 , with its wide bandgap and catalytically near-passive surface, is a model substrate for engineering bandgap and inducing additional properties through introducing catalytically active surface sites by incorporation of foreign metal ions. For example, incorporation of both Ce^{4+} and Fe^{3+} successfully narrowed down the bandgap of CaWO_4 and created catalytically active sites for visible-light applications such as photo-Fenton catalytic degradation.²¹ In the case of Eu^{3+} -incorporated CaWO_4 , instead of narrowing bandgap, Eu^{3+}

sites on the surface served to improve adsorption by raising the d-band centre and initiating photodegradation processes for organic pollutants under ultra-violet (UV) light.²² Such a strategy of inducing catalytic active sites could also be applied to development of CaWO₄-based electrocatalysts. This is particularly true for the electrocatalysts used in sensing applications since the facile synthesis of mixed CaWO₄ could contribute to the preparation of low-cost and disposable electrodes (e.g. determination of glucose concentration), one of the key components for sensing.²³ However, the related research has been limited so far.

Quantitative determination of glucose content is important for food analysis, quality assurance, and blood glucose monitoring.²⁴ In order to perform spectroscopic analysis, glucose must first be functionalised with chromophores or fluorophores.²⁵ An alternative approach is electrochemical sensing, where the glucose molecules are oxidised to produce a signal.²⁶ Enzymatic glucose electrooxidation has been a popular approach due to its greater accuracy and high sensitivity.²⁷ However, enzymes are often vulnerable to environmental parameters (e.g. temperature, pH value, and humidity etc.) during electrochemical measurements.²⁸ Non-enzymatic glucose electrooxidation by metal oxides has, thus, attracted great attention due to the stability of catalysts, simple electrode design, and broad application potentials, though with comparatively lower selectivity.²⁹ A plethora of transition metal oxides and mixed metal oxides was reported to exhibit formidable catalytic activities for non-enzymatic electrooxidation of glucose.³⁰ Notably, Mn-containing metal oxides, such as α -MnO₂³¹ and Mn-doped NiO³², achieved high sensitivity, low limit of detection, and broad linear detection range, featuring the important role of Mn as the catalytically active component in this type of materials.

In this work, we present a series of Ca_{1-x}Mn_xWO₄ compounds with high crystallinity prepared via a facile co-precipitation method at low temperature (30 °C) for electrooxidation of glucose. These Ca_{1-x}Mn_xWO₄ compounds are thoroughly investigated by a broad range of

characterisation techniques. We further demonstrate a stark improvement in the catalytic activity for electrooxidation of glucose due to the incorporation of Mn^{2+} in CaWO_4 , an example of a completely new property being introduced to the host material following metal ion integration.

Experimental

Materials

All materials were used as received, without further purifications. $\text{Na}_2\text{WO}_4 \cdot 2\text{H}_2\text{O}$, anhydrous CaCl_2 , Nafion D-520 (5% w/w in H_2O /isopropanol), NaOH , HPLC-grade water, and glucose were purchased from Fisher Scientific. $\text{MnCl}_2 \cdot 4\text{H}_2\text{O}$ was purchased from VWR international. Deionised water was used throughout the experimental activities unless specified otherwise.

Synthesis of Mn-incorporated CaWO_4

Mn-incorporated CaWO_4 compounds were synthesised via co-precipitation of M^{2+} (Ca^{2+} , Mn^{2+}) and WO_4^{2-} ions in an aqueous medium. A 1:1 ratio was maintained between WO_4^{2-} and the M^{2+} ions throughout the synthesis procedures. CaCl_2 , $\text{MnCl}_2 \cdot 4\text{H}_2\text{O}$, and $\text{Na}_2\text{WO}_4 \cdot 2\text{H}_2\text{O}$ were used as precursors to the desired ions. Anhydrous CaCl_2 was mixed with $\text{MnCl}_2 \cdot 4\text{H}_2\text{O}$ at varying ratios to make up a total of 8 mmol M^{2+} , and dissolved in deionised water (15 mL) in a beaker. The Mn concentration is defined as $(\text{Mn}_{\text{mol}}/[\text{Mn}_{\text{mol}}+\text{Ca}_{\text{mol}}])$. $\text{Na}_2\text{WO}_4 \cdot 2\text{H}_2\text{O}$ (8 mmol, 2.6388 g) was dissolved in deionised water (15 mL) in another beaker. The solution containing Mn^{2+} and Ca^{2+} was added slowly into the Na_2WO_4 solution under vigorous magnetic stirring. Immediate formation of white (yellowish with the addition of Mn precursor in the synthesis) precipitates was observed. The magnetic stirring of the mixture continued for 15 minutes. The resulting mixture was allowed to settle and kept at 30 ± 2 °C in an oven for over 24 hours. The precipitates were treated through cycles of centrifugation, decanting the supernatant, and re-

dispersion in deionised water for purification. This process was repeated until the pH value of the supernatant is equal to that of deionised water. The purified precipitates were then washed with ethanol twice and allowed to dry in ambient room temperature.

Characterisations

Powder X-ray diffraction patterns were collected using a Malvern Panalytical Empyrean X-ray diffractometer with a copper X-ray tube as the X-ray source ($\lambda = 0.154184$ nm). The size of crystal grains was estimated using the diffraction peak of (101) plane via Scherrer equation, $D = k\lambda/\beta(\cos\theta)$, in which D is the average size of crystal grains, k represents Scherrer constant (commonly taken as 0.9), λ is the wavelength of the X-ray, β is the full width half maximum (FWHM) adjusted for instrumental broadening in radians, and θ is the Bragg angle.³³ The diffraction peaks were fitted using the pseudo-Voigt 2 function on Origin to find the corresponding FWHMs and 2θ . Scanning electron microscopic (SEM) images were acquired using a Hitachi S-4700 scanning electron microscope. The samples were dispersed in ethanol by sonication, drop-cast onto a clean silicon wafer, dried in air overnight, attached to a sample holder, and sputter coated with a thin layer of gold prior to imaging. Transmission electron microscopic (TEM) images were collected by using a Hitachi H-7500 transmission electron microscope. High resolution transmission electron microscopic (HRTEM) imaging and energy dispersive X-ray (EDX) spectroscopic mapping were carried out using a JEOL JEM2100F transmission electron microscope equipped with an Oxford instruments INCA Energy TEM 250 detector. Fourier transform infrared spectroscopy (FT-IR) was carried out on a Perkin-Elmer Frontier spectrometer, through the use of CsI pellets. CsI pellets used for infra-red spectra were obtained by grinding anhydrous CsI (200 mg) and sample (2 mg) together using a mortar and pestle, and pressing them into a pellet in a pellet mould using 10 T of force on a hydraulic press. The metal elements in the samples were quantitatively analysed by an

inductively coupled plasma optical emission spectroscopic (ICP-OES) technique on an Agilent 5110 ICP-OES. X-ray photoelectron spectra (XPS) were acquired on a SPECS spectrometer with a non-monochromatic Al and Mg X-ray source operating at 200 W. The spectrometer is equipped with a Phoibos 150 MCD-9 detector. The XPS peaks were deconvoluted by using XPSPEAK Version 4.1 developed by Raymond W. M. Kwok. The peaks were fitted to asymmetric Gaussian-Lorentzian sum functions with nonlinear Shirley background subtractions. The binding energies in both experimental and fitted XPS spectra were calibrated with respect to C 1s (C-C) peak at 284.8 eV from the measured adventitious carbon.

Electrochemical measurements

Electrochemical glucose oxidation was performed using a PalmSens3 portable potentiostat in a 3-electrode single cell system with 0.1 M NaOH solution as the electrolyte. Electrodes were manufactured by CH Instruments. A glassy carbon electrode (GCE, CHI104, 3 mm diameter, 0.071 cm²) modified with catalyst ink served as the working electrode while Pt wire (CHI115) was employed as the counter electrode. A Hg/HgO electrode (CHI152) is chosen as the reference electrode due to the alkaline medium of the measurement system. The catalyst ink was prepared as following: 10 mg Mn-incorporated CaWO₄ was dispersed in 750 μL HPLC-grade water by sonication for over 1 h. 20 μL Nafion D-520 solution was mixed into 250 μL ethanol, and the resulting mixture was then added into the above sample suspension under sonication to obtain the final ink. 3 μL final ink was drop-cast onto the freshly polished GCE surface, and dried under an infrared lamp. This procedure leads to a catalyst loading approximately at 0.42 mg·cm⁻². All measurements were performed in a 10 mL electrochemical cell. Current densities are calculated based on the geometric surface area of the GCE. The reported potentials were converted to reversible hydrogen electrode (RHE) scale using the following equation: $E_{RHE} = E_{Hg/HgO} + (0.0591 * pH) + 0.098$. Cyclic Voltammetry (CV) was used

to determine the catalytic activities of the Mn-incorporated CaWO_4 toward glucose. Data were collected from 0.87 to 1.67 V vs. RHE at $0.05 \text{ V}\cdot\text{s}^{-1}$. Chronoamperometry at 0.97 V vs. RHE, with a data collection interval of 3 s, was used to find the sensitivity of the catalyst for an oxidation process. The amperometric response to increased glucose concentrations was monitored for the 0.002–1 mM range. Incremental increases of the glucose concentration were achieved by sequentially adding small and precise aliquots (10–53 μL) of freshly made glucose stock solutions (glucose in 0.1 M NaOH), with taking the final volume of the cell into account, to the electrolyte solution of the three-electrode setup. See Table S1 for the detail. The electrochemical system was allowed to equilibrate for 60 min prior to addition of the first aliquot of glucose stock.

Results and Discussion

Characterisation of $\text{Ca}_{1-x}\text{Mn}_x\text{WO}_4$

A series of Mn-incorporated CaWO_4 was synthesised through a co-precipitation method at $30 \pm 2 \text{ }^\circ\text{C}$. The accurate compositions of metallic elements for the samples were analysed via inductively coupled plasma optical emission spectroscopic (ICP-OES) measurements, which revealed that the Mn content in each sample was slightly higher than that in the precursors (Table 1). This phenomenon is explained by the fact that precipitation yields for the precursors are not 100%, as well as the fact that there is a significant difference in the solubility product constants (K_{sp}) of CaWO_4 and MnWO_4 .^{34,35} This means Mn^{2+} demonstrates much higher affinity for tungstate ions (WO_4^{2-}) than Ca^{2+} , and, therefore, Mn tends to be over-represented

in the final samples for this synthetic approach. Furthermore, the molar ratio of (Ca + Mn):W in all the as-prepared samples is greater than the stoichiometric ratio of 1. Similar observations were reported for $\text{Ca}_{1-x}\text{Zn}_x\text{WO}_4$ and ZnWO_4 nanocrystals with thorough investigations.^{6,9} For these materials, the excessive Ca and Zn were proven to occur at the surface of the nanocrystals where the surface adsorbed citric and/or diglycol species, as well as surface hydration layers, were found to be responsible for the surface nonstoichiometry.^{6,9} The following characterisation results will corroborate the surface-related nature of the nonstoichiometry for the current $\text{Ca}_{1-x}\text{Mn}_x\text{WO}_4$ compounds.

Table 1. Compositions of Ca, Mn, and W in $\text{Ca}_{1-x}\text{Mn}_x\text{WO}_4$ measured by ICP-OES

Molar ratios in precursors $\text{Ca}^{2+} : \text{Mn}^{2+} : \text{W}^{6+}$	Molar ratios determined by ICP-OES $n \times (\text{Ca} : \text{Mn}) : \text{W}$	Final formula in $\text{Ca}_{1-x}\text{Mn}_x\text{WO}_4$ form*
1.000 : 0.000 : 1	$2.756 \times (1.000 : 0.000) : 1$	CaWO_4
0.975 : 0.025 : 1	$1.100 \times (0.967 : 0.033) : 1$	$\text{Ca}_{0.967}\text{Mn}_{0.033}\text{WO}_4$
0.950 : 0.050 : 1	$1.114 \times (0.938 : 0.062) : 1$	$\text{Ca}_{0.938}\text{Mn}_{0.062}\text{WO}_4$
0.925 : 0.075 : 1	$1.035 \times (0.907 : 0.093) : 1$	$\text{Ca}_{0.907}\text{Mn}_{0.093}\text{WO}_4$
0.900 : 0.100 : 1	$1.022 \times (0.876 : 0.124) : 1$	$\text{Ca}_{0.876}\text{Mn}_{0.124}\text{WO}_4$
0.875 : 0.125 : 1	$1.085 \times (0.847 : 0.153) : 1$	$\text{Ca}_{0.847}\text{Mn}_{0.153}\text{WO}_4$
0.850 : 0.150 : 1	$1.083 \times (0.817 : 0.183) : 1$	$\text{Ca}_{0.817}\text{Mn}_{0.183}\text{WO}_4$
0.825 : 0.175 : 1	$1.042 \times (0.790 : 0.210) : 1$	$\text{Ca}_{0.790}\text{Mn}_{0.210}\text{WO}_4$
0.800 : 0.200 : 1	$1.045 \times (0.759 : 0.241) : 1$	$\text{Ca}_{0.759}\text{Mn}_{0.241}\text{WO}_4$
0.790 : 0.210 : 1	$1.038 \times (0.721 : 0.279) : 1$	$\text{Ca}_{0.721}\text{Mn}_{0.279}\text{WO}_4$

*($\text{Ca}_{1-x}\text{Mn}_x$)_n WO_4 is noted in a formula of $\text{Ca}_{1-x}\text{Mn}_x\text{WO}_4$ for convenience.

The powder X-ray diffraction (PXRD) pattern of as-prepared CaWO_4 without Mn-incorporations is shown in Figure 1. The pattern matches that of a bulk CaWO_4 with a tetrahedral scheelite structure belonging to $I4_1/a$ space group (ICDD PDF No. 00-041-1431).³⁶ No additional diffraction peaks are observed, demonstrating the high purity of the crystal phase.

Upon introducing Mn^{2+} into the precursors, the tetrahedral scheelite structure is retained for the final compounds with increasing the Mn^{2+} content in the precursors up to 20% ($\text{Mn}_{\text{mol}}/[\text{Mn}_{\text{mol}}+\text{Ca}_{\text{mol}}]$), which corresponds to 24.1% Mn in the final compound ($\text{Ca}_{0.759}\text{Mn}_{0.241}\text{WO}_4$ in Figure 1 and S1). Further increasing the Mn^{2+} content in the precursors by 1% leads to the emergence of several new diffraction peaks (Figure S2) that are not from tetrahedral scheelite, implying the solid solubility limit of Mn in CaWO_4 is $\sim 24\%$ for the current co-precipitation method.

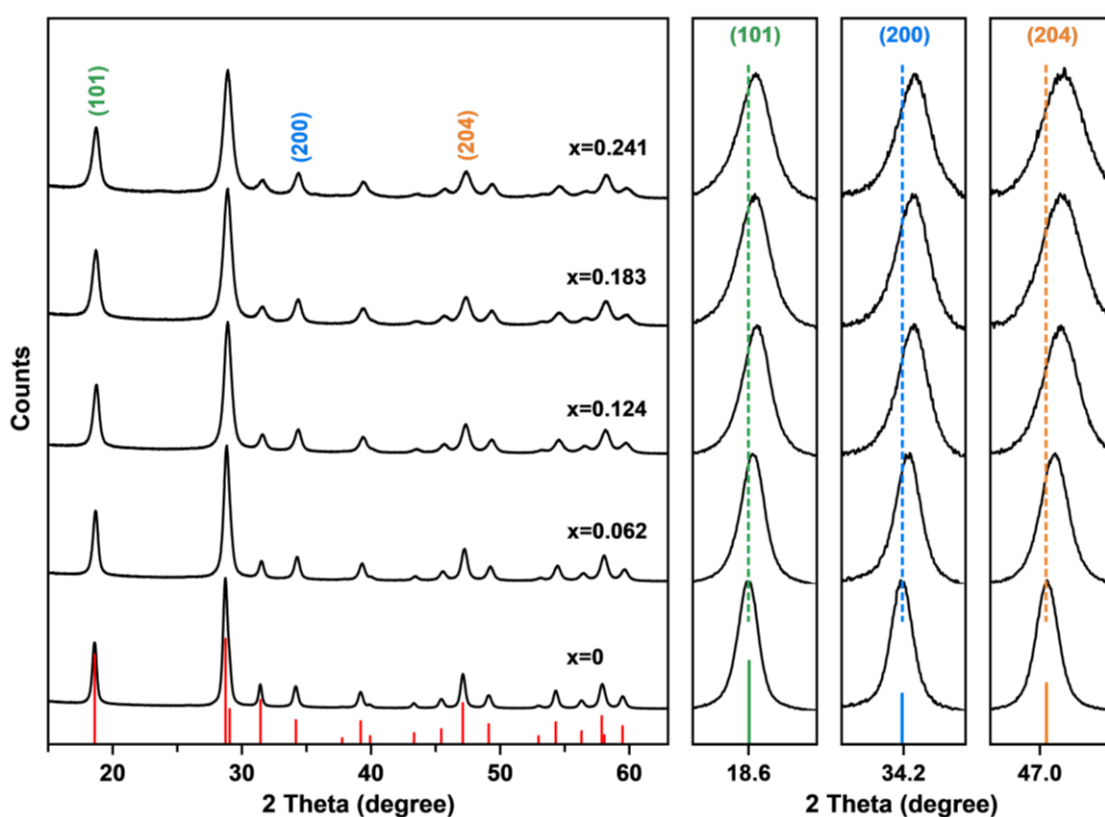


Figure 1. Powder X-ray diffraction patterns of $\text{Ca}_{1-x}\text{Mn}_x\text{WO}_4$, where $x = 0, 0.062, 0.124, 0.183,$ and 0.241 , corresponding to the Mn content at 0.000, 0.050, 0.100, 0.150, and 0.200 in the precursors, respectively. The diffractions peaks of (101), (200), and (204) crystal planes are magnified to show the gradual shifts. The vertical solid bars represent the reference data for bulk CaWO_4 (ICDD PDF No. 00-041-1431). The vertical dotted lines are employed to highlight the peak shifts. A full set of XRD patterns is given in Figure S1.

Interestingly, compared to the diffraction peaks of as-prepared CaWO_4 , various degrees of shifts toward higher angles are observed for the diffraction peaks of Mn-incorporated CaWO_4 . In particular, within an individual PXRD pattern of a given $\text{Ca}_{1-x}\text{Mn}_x\text{WO}_4$, the magnitude of the shifts gets greater with the increase of diffraction angles. For a given diffraction peak, the magnitude of the shifts increases with increasing the Mn content in $\text{Ca}_{1-x}\text{Mn}_x\text{WO}_4$. These observations are visualised via the zoomed-in diffraction peaks of (101), (200), and (204) crystal planes at around 18.6, 34.2, and 47.1 degrees, respectively, in Figure 1. The shifts in the diffraction peaks toward higher diffraction angles imply gradual lattice contractions of $\text{Ca}_{1-x}\text{Mn}_x\text{WO}_4$ with increasing Mn content, which is expected when larger cations (Ca^{2+} , 1.12 Å, coordination number, CN = 8)³⁷ are gradually substituted by smaller ones (Mn^{2+} , 0.96 Å, CN = 8)³⁷ in a crystal lattice.⁶

The structural changes are further investigated quantitatively via least squares Rietveld structural refinement using General Structure Analysis System II (GSAS II) software.^{38,39} Figure 2a shows representative Rietveld refinement results for the PXRD patterns of as-prepared CaWO_4 and $\text{Ca}_{0.876}\text{Mn}_{0.124}\text{WO}_4$, which were refined based on initial parameters reported previously.⁴⁰ The simulated patterns in Figure 2a are in excellent agreement with experimental ones for both samples as indicated by the corresponding low overall weighted profile residual (wR) and goodness of fit (χ^2).⁴¹ Such excellent fittings between simulated and measured patterns are repeated in the Rietveld refinements for the rest of the $\text{Ca}_{1-x}\text{Mn}_x\text{WO}_4$ compounds, and all the refined details are summarised in Table S2. Evidently, the unit cell parameters (a and c) of $\text{Ca}_{1-x}\text{Mn}_x\text{WO}_4$ follow Vegard's law and vary linearly as a function of Mn content (Figure S3).⁴² The unit cell volumes of $\text{Ca}_{1-x}\text{Mn}_x\text{WO}_4$ are, therefore, calculated and plotted as a function of Mn content in Figure 2b.

Increasing the Mn content from 0 to 24.1% leads to a monotonous reduction in cell volume. The trend of lattice contraction is halted with further increasing Mn content to 27.9%, and the corresponding cell volume stays at the level in between those of the compounds with 21.0% and 24.1% Mn, further confirming the solid solubility limit (~24%) of Mn in CaWO_4 observed from the PXRD patterns in Figure 1, S1, and S2. Note that the linearity of the lattice contraction with increasing Mn content is slightly skewed by the unevenly exerted size effects on the lattice cells due to varied crystal grain sizes among the series of $\text{Ca}_{1-x}\text{Mn}_x\text{WO}_4$ samples (Table S3). Lattice expansions along crystal grain size reductions were well reported previously for tungstate materials such as CaWO_4 , CdWO_4 , ZnWO_4 , and MnWO_4 .^{9,10,43,44} Probing the changes in axis ratios of c/a with increasing Mn content could provide further insights to the lattice contraction. The axis ratio of c/a in Figure 2b exhibits little to no change (between 2.1695 and 2.1704) with increasing Mn content, indicating that the lattice contraction is isotropic. A similar finding was reported and carefully discussed for $\text{Ca}_{1-x}\text{Zn}_x\text{WO}_4$ nanocrystals, where the physical rigidity led to wholistic movements of WO_4 tetrahedra equivalently along the a - and c -axis during the lattice contraction.⁶ One can reasonably expect the same is true for the current $\text{Ca}_{1-x}\text{Mn}_x\text{WO}_4$ compounds.

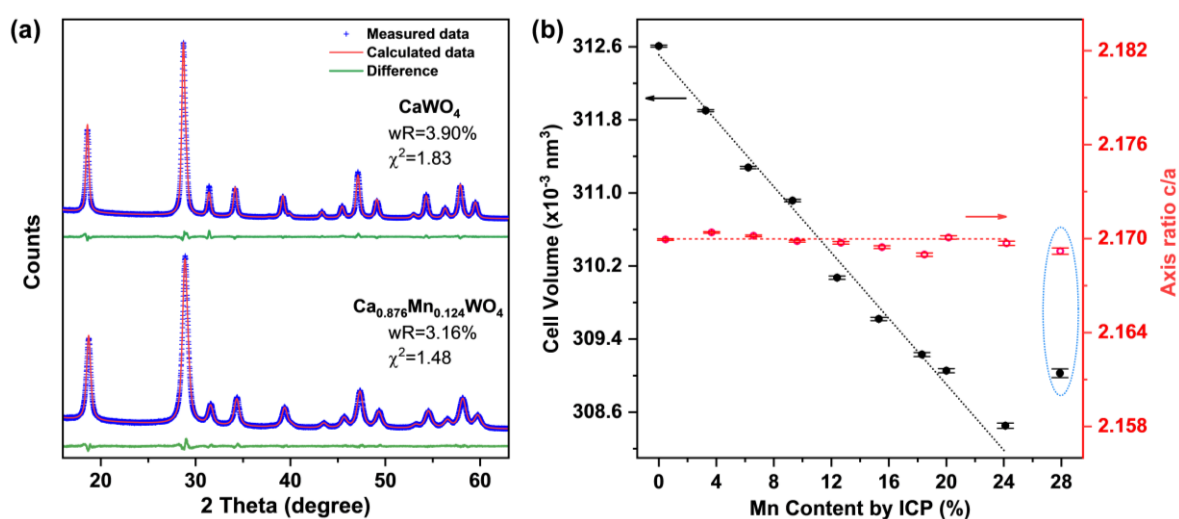


Figure 2. (a) Rietveld fittings of the PXRD patterns of as-prepared CaWO_4 and $\text{Ca}_{0.876}\text{Mn}_{0.124}\text{WO}_4$, (b) cell volume and axis ratio c/a as a function of Mn content in $\text{Ca}_{1-x}\text{Mn}_x\text{WO}_4$. The dotted lines in (b) show the trends of the data. The circle in (b) highlights the data points for $\text{Ca}_{0.721}\text{Mn}_{0.279}\text{WO}_4$.

The scanning electron microscopic (SEM) images in Figure 3a and S4a show a sphere-like structure for the as-prepared CaWO_4 , with the size (“diameter”) broadly ranging from submicron up to $\sim 3 \mu\text{m}$. There are also small aggregates with irregular shapes as the minor component to the overall morphologies. Upon a closer inspection, the spheres are, in fact, assemblies of small nanocrystals as exhibited in the transmission electron micrograph (TEM) and SEM images in Figure 3a and S4b, respectively. The lattice spacing, 0.288 nm, measured and highlighted in the high-resolution TEM (HRTEM) image in Figure 3a matches well the corresponding d -spacing of (004) plane. The nanocrystal in the HRTEM image in Figure 3a has a surface amorphous layer with ~ 2 nm thickness, which is likely associated with the surface nonstoichiometry observed in the ICP-OES measurements in Table 1.¹⁴ Such surface amorphous layers are consistently seen in the as-prepared CaWO_4 (Figure S4). With the addition of Mn into the precursors, the sphere-like structures of the assembled nanocrystals are partially dismantled to smaller sphere-like structures and fragmented aggregates of the nanocrystals as demonstrated in the representative SEM and TEM images of $\text{Ca}_{0.759}\text{Mn}_{0.241}\text{WO}_4$ in Figure 3b. The size of sphere-like structures is drastically reduced to the range below $1 \mu\text{m}$, with the sphere-like geometry becoming poorly defined as evidenced by the corresponding SEM images of $\text{Ca}_{0.759}\text{Mn}_{0.241}\text{WO}_4$, $\text{Ca}_{0.876}\text{Mn}_{0.124}\text{WO}_4$, and $\text{Ca}_{0.817}\text{Mn}_{0.183}\text{WO}_4$ in Figure 3b and S6, respectively. The lattice spacing (0.315 nm) of $\text{Ca}_{0.759}\text{Mn}_{0.241}\text{WO}_4$ corresponds to the d -spacing of (112) plane as shown in the HRTEM image in Figure 3a, with surface amorphous layers being frequently seen.

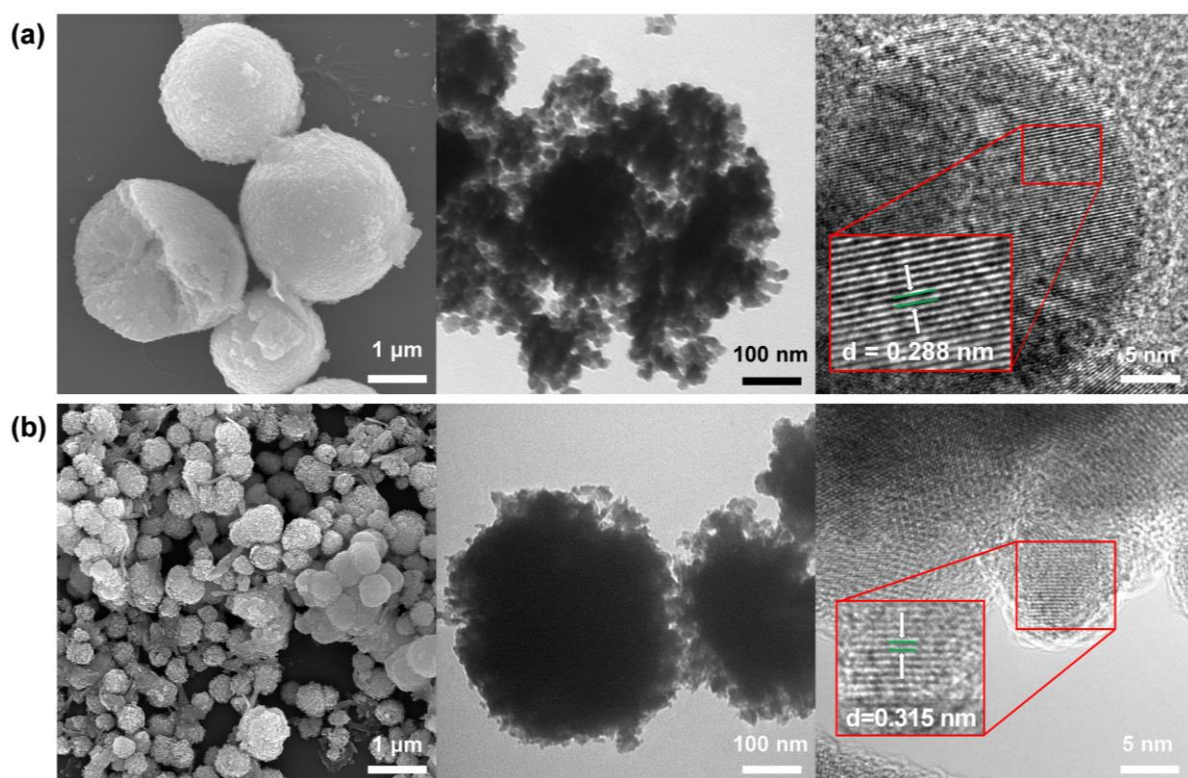


Figure 3. Representative SEM, TEM, and HRTEM images of (a) CaWO_4 and (b) $\text{Ca}_{0.759}\text{Mn}_{0.241}\text{WO}_4$.

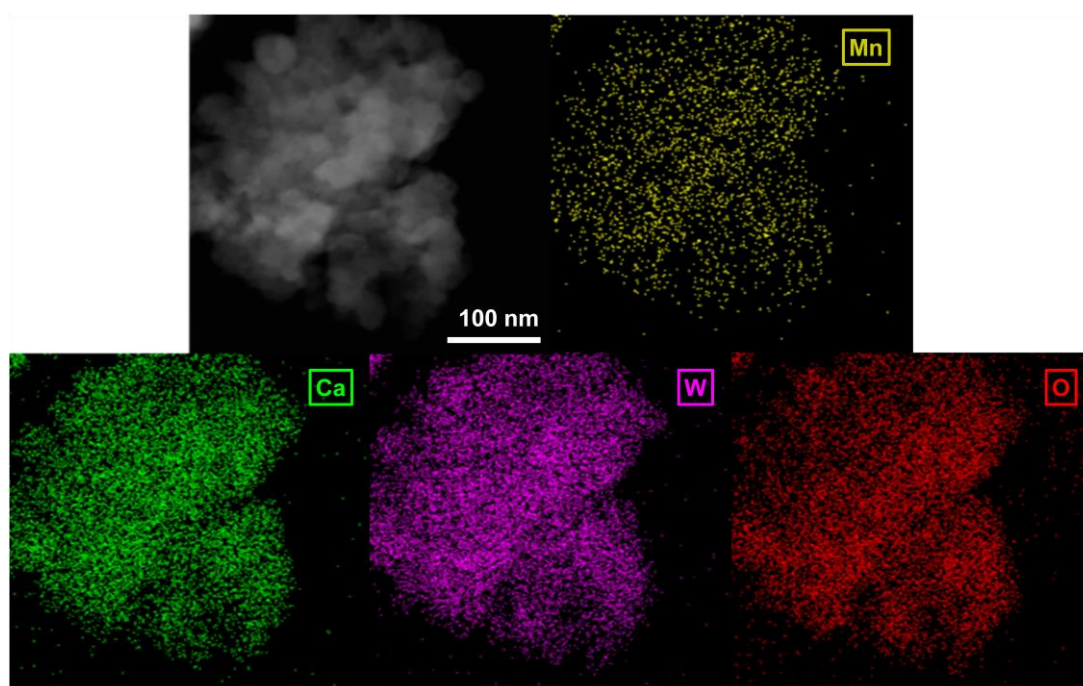


Figure 4. TEM-EDX elemental mapping for $\text{Ca}_{0.759}\text{Mn}_{0.241}\text{WO}_4$.

Elemental analyses such as energy dispersive X-ray (EDX) elemental mapping and X-ray photoelectron spectroscopic techniques are carried out to further confirm the incorporation of Mn into CaWO_4 lattices (distribution) and the substitution of Ca by Mn (oxidation state). The representative results of the TEM-EDX mapping for $\text{Ca}_{0.759}\text{Mn}_{0.241}\text{WO}_4$ are given in Figure 4. The relevant elements such as Mn, Ca, W, and O are all readily detected with even distributions over the targeted sample area. More importantly, no agglomeration of Mn is observed, and the distribution of Mn overlaps well with that of Ca, W, and O.

XPS measurements are carried out to as-prepared CaWO_4 , $\text{Ca}_{0.876}\text{Mn}_{0.124}\text{WO}_4$, and $\text{Ca}_{0.759}\text{Mn}_{0.241}\text{WO}_4$. Figure 5a shows the corresponding Ca 2p spectra where all three compounds demonstrate Ca 2p_{3/2} and Ca 2p_{1/2} peaks located consistently at 347.1 and 350.6 eV, respectively. These binding energies are very close to those of Ca^{2+} in CaWO_4 reported previously.⁴⁵ For the XPS spectra of W 4f, both W 4f_{7/2} and W 4f_{5/2} peaks are fitted, respectively, to the sum of two peaks (Figure 5b). The main peaks at ~35.6 and ~37.9 eV are related to W^{6+} while the two minor peaks at ~34.6 and ~36.8 eV are associated with W^{5+} . The binding energies for W^{6+} are in good agreement with the data in the past studies for commercial WO_3 and nanocrystalline CaWO_4 films.^{46,47} The presence of W^{5+} along with W^{6+} have been described to exist in various materials such as WO_3 and $\text{W}_{18}\text{O}_{49}$.^{46,48} All O 1s spectra in Figure 5c are deconvoluted into three peaks with the main peak located at ~530.7 eV, which is associated with lattice oxygens in tungstate compounds.⁴⁹ The minor peak located at ~532.1 eV is attributed to surface hydroxyl groups that originate from the chemisorbed surface water, passivated surface oxygen atoms by the adsorbed surface hydrogen species, and/or the hydroxyl groups resulted from water healing/oxidising surface oxygen vacancies.⁴⁹⁻⁵¹ The remaining minor peak at ~533.3 eV corresponds to physisorbed surface water molecules with loose bonding to the surface.^{50,52}

Figure 5d shows XPS Mn 2p spectra of $\text{Ca}_{0.876}\text{Mn}_{0.124}\text{WO}_4$, and $\text{Ca}_{0.759}\text{Mn}_{0.241}\text{WO}_4$, of which the spectral shapes and binding energies closely resemble those reported for Mn in MnWO_4 .⁵³ The two Mn 2p spectra feature Mn 2p_{3/2} and Mn 2p_{1/2} peaks, as well as their corresponding satellite peaks. Both Mn 2p_{3/2} and Mn 2p_{1/2} peaks are individually deconvoluted into two peaks. The two dominant peaks located at ~641.5 and ~653.4 eV are consistent with the doublets of Mn^{2+} , with the two minor doublets at ~643.6 and ~655.3 eV being assigned to Mn^{3+} .⁵⁴ This further confirms the substitution of Ca by Mn. The presence of Mn^{3+} neatly negates the charge imbalance brought by the existence of W^{5+} . However, the existence of W^{5+} in the as-prepared CaWO_4 ($x = 0$) means that the charge imbalance cannot be compensated solely by Mn^{3+} . Instead, a portion of surface excessive Ca^{2+} ions, along with the surface hydration layers (based on the XPS O 1s spectra in Figure 5c), could potentially fulfil the charge-balancing role. This also explains the unusual surface excessiveness of CaWO_4 ($n = 2.756$ in Table 1) compared to that of Mn-incorporated CaWO_4 compounds.

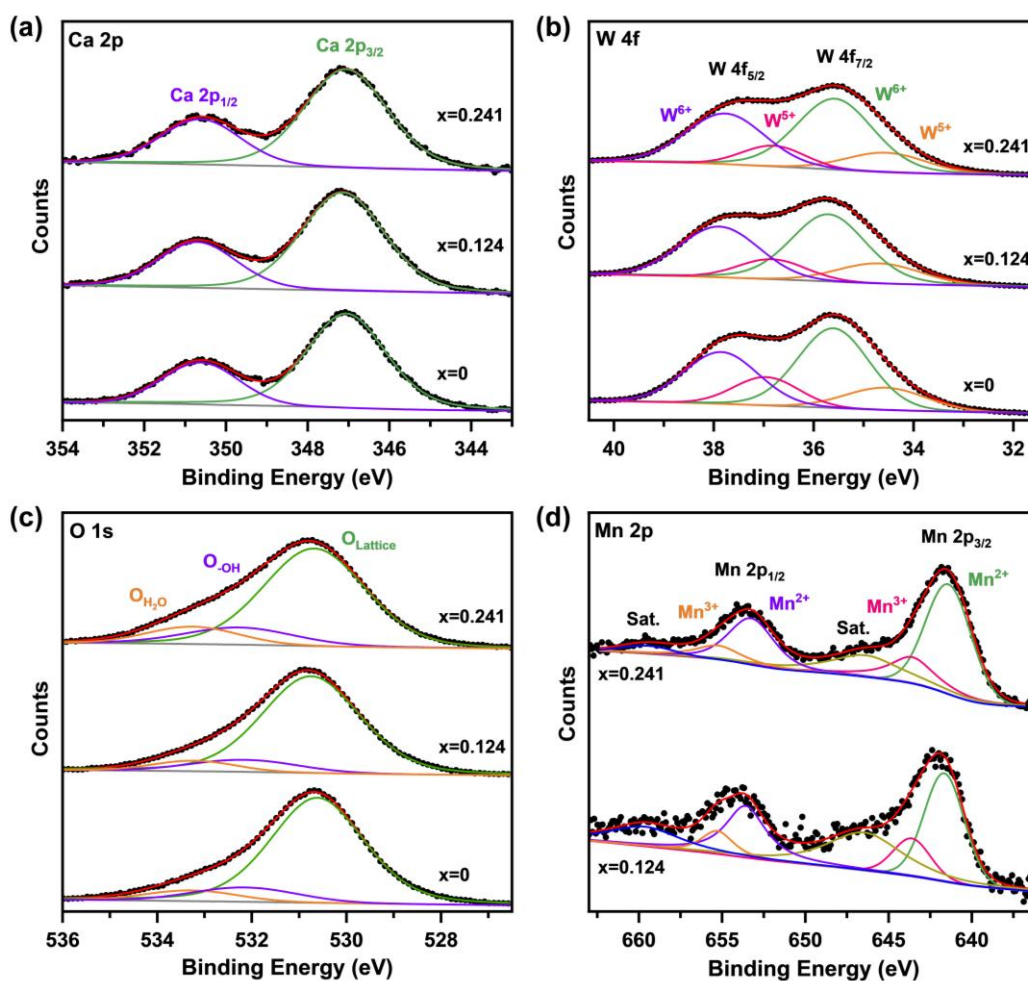


Figure 5. XPS (a) Ca 2p, (b) W 4f, and (c) O 1s spectra of as-prepared CaWO_4 , $\text{Ca}_{0.876}\text{Mn}_{0.124}\text{WO}_4$, and $\text{Ca}_{0.759}\text{Mn}_{0.241}\text{WO}_4$, and (d) XPS Mn 2p spectra of $\text{Ca}_{0.876}\text{Mn}_{0.124}\text{WO}_4$, and $\text{Ca}_{0.759}\text{Mn}_{0.241}\text{WO}_4$ (d).

Vibrational properties and surface chemistry of $\text{Ca}_{1-x}\text{Mn}_x\text{WO}_4$ are investigated by Fourier-transform infrared (FT-IR) spectroscopy. The full spectra of all $\text{Ca}_{1-x}\text{Mn}_x\text{WO}_4$ compounds are given in Figure S7. It is evident that the absorption bands are distributed in four regions, for which corresponding zoomed-in sections are shown in Figure 6. The bands at ~ 3435 and ~ 1635 cm^{-1} are the absorptions from the stretching of H-O bonds and bending of H-O-H, respectively, from the water molecules of surface the hydration layers.^{6,10,44} The absorption bands below 1000 cm^{-1} are characteristic to CaWO_4 .^{55,56} The stretching vibrations of WO_4^{2-} lead to strong absorptions at ~ 795 and ~ 860 cm^{-1} .⁵⁶⁻⁵⁸ A shoulder band at ~ 918 cm^{-1} is observed for all the

samples and it is attributed to the surface disorder layers of small nanocrystals.^{10,11} Note that the so-called surface disorder layers are still crystalline (the surface section of crystals) and, therefore, are different from the surface nonstoichiometric layers that are highly likely amorphous as shown in the TEM images in Figure 3. The band located at $\sim 439\text{ cm}^{-1}$ is attributed to the absorption due to WO_4^{2-} bending.^{57,58} The band energy blueshifts slightly from 439 to 443 cm^{-1} with increasing Mn content from 0 to 24.1% as indicated by the blue dotted line in Figure 6, likely owing to the lattice contraction.^{43,44}

For the absorptions in the range between $360\text{ to }260\text{ cm}^{-1}$, the broad peak can be seen as an overlapping of three bands at ~ 341 (shoulder), ~ 320 (main), and ~ 279 (minor) cm^{-1} as highlighted by the red dotted rectangle in Figure 6, which are associated with rotations of WO_4^{2-} .⁵⁹ Interestingly, these three peaks become less and less defined and eventually merge into a broad peak with increasing the Mn content. The overlapping of the three absorptions is somewhat close to that of a $\text{CaWO}_4:\text{Nd}^{3+}$ single crystal reported in the literature, where the shoulder and the minor peaks, located at ~ 279 and $\sim 341\text{ cm}^{-1}$ respectively, were reversed compared to the present study.⁶⁰ The absorption band at $\sim 219\text{ cm}^{-1}$ is associated with rotations of WO_4^{2-} .^{57,59} The above FT-IR analyses corroborate the existence of considerable quantities of the surface hydration species as indicated by the XPS O 1s spectra in Figure 5c. The blueshift and merging of FT-IR peaks corroborate the structural changes revealed in the Rietveld refinements in Figure 2, Table S1, and Figure S3.

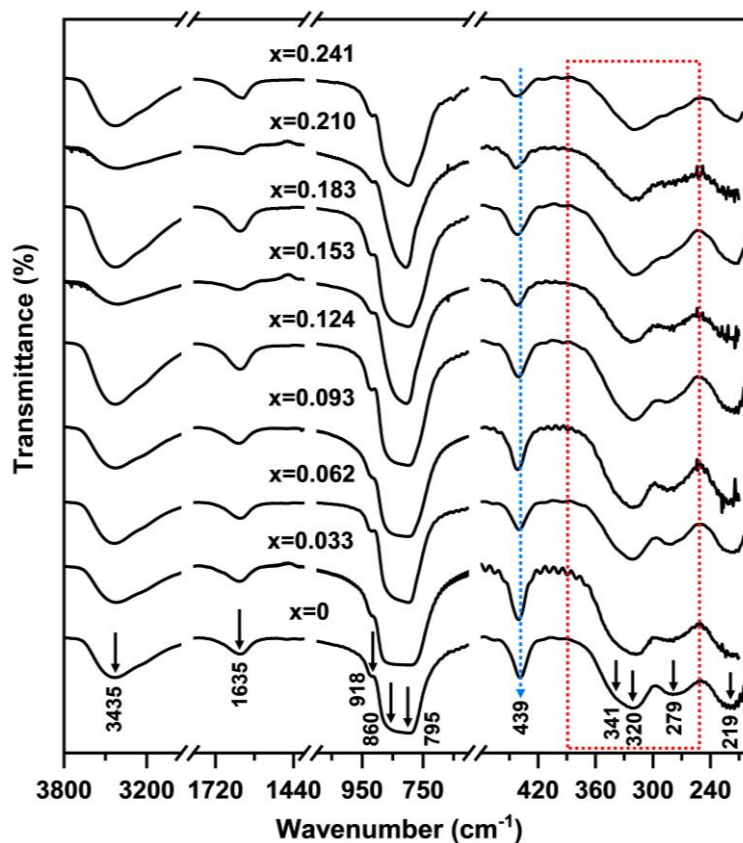


Figure 6. FT-IR spectra of $\text{Ca}_{1-x}\text{Mn}_x\text{WO}_4$ with the regions of vibrational bands highlighted. The dotted line and rectangle highlight the changes occurring to the corresponding absorption bands with increasing Mn content.

Nonenzymatic glucose electrooxidation

Cyclic voltammetry (CV) is performed for the initial investigation of the electrochemical response of $\text{Ca}_{1-x}\text{Mn}_x\text{WO}_4$ coated glassy carbon electrodes (GCE) to glucose (5 mM) in a 0.1 M NaOH electrolyte solution. The cyclic voltammograms of $\text{Ca}_{1-x}\text{Mn}_x\text{WO}_4$ GCEs in Figure 7a and S8a all feature two oxidation peaks in the regions of 0.85 – 1.20 V and 1.30 – 1.7 V vs RHE, respectively, for the anodic scans. The current densities of the two peaks increase with increasing the Mn content in CaWO_4 . Additionally, the corresponding peak potentials shift positively with increasing the Mn content (general trend). Note that the shape of the cyclic

voltammogram for $\text{Ca}_{0.759}\text{Mn}_{0.241}\text{WO}_4$ coated GCE resembles that of CVs with platinum nanoparticles in neutral medium and gold nanoparticles in 0.1 M NaOH,^{26,61} which is different from a single oxidation peak commonly reported for metal oxides/hydroxides in electrochemical glucose oxidations.^{62,63} In comparison, no oxidation peak is observable for the CV of CaWO_4 coated GEC, indicating a different electrochemical behaviour to that of GCEs coated with Mn-incorporated CaWO_4 materials (Figure 7a and S8a).

The CVs of CaWO_4 and $\text{Ca}_{0.759}\text{Mn}_{0.241}\text{WO}_4$ coated GCEs are compared to that of a clean GCE with no coating under the same condition in Figure S8b, which clearly shows a direct link between the emergence of the two oxidation peaks and the presence of Mn element in CaWO_4 . Figure 7b and S9 show CVs of $\text{Ca}_{0.759}\text{Mn}_{0.241}\text{WO}_4$, CaWO_4 , $\text{Ca}_{0.938}\text{Mn}_{0.062}\text{WO}_4$, and $\text{Ca}_{0.876}\text{Mn}_{0.124}\text{WO}_4$ coated GCEs in 0.1 M NaOH with and without the presence of 5 mM glucose. No obvious glucose oxidation peak was observed for the CaWO_4 coated GCE when comparing the two CVs in Figure S9a while the oxidation peak start to emerge for the $\text{Ca}_{0.938}\text{Mn}_{0.062}\text{WO}_4$ coated GCE with the presence of glucose (Figure S9b). The significantly pronounced oxidation peaks are observed for the both $\text{Ca}_{0.759}\text{Mn}_{0.241}\text{WO}_4$ (Figure 7b) and $\text{Ca}_{0.876}\text{Mn}_{0.124}\text{WO}_4$ (Figure S9c) coated GCEs, which are clearly associated with the presence of glucose. This establishes the basis for glucose sensing via electrochemical oxidation by CaWO_4 with high Mn content in this work.

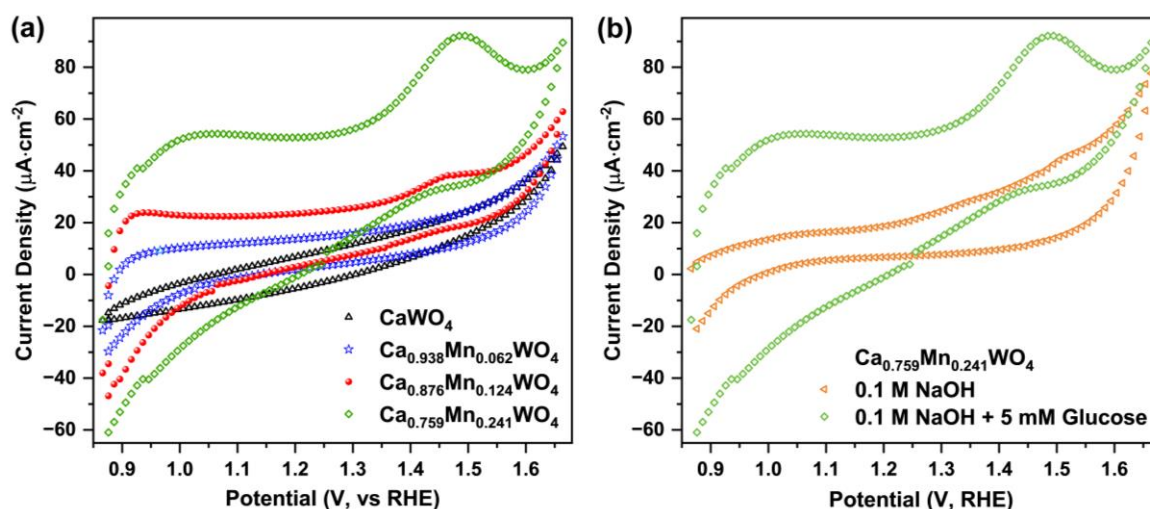


Figure 7. (a) Cyclic voltammograms of $\text{Ca}_{1-x}\text{Mn}_x\text{WO}_4$ ($x = 0, 0.062, 0.124, \text{ and } 0.241$) coated GCEs in 0.1 M NaOH and 5 mM glucose, and (b) Cyclic voltammograms of $\text{Ca}_{0.759}\text{Mn}_{0.241}\text{WO}_4$ coated GCE in 0.1 M NaOH with and without the presence of 5 mM glucose. The scanning rate is set at $50 \text{ mV} \cdot \text{s}^{-1}$ for all the CVs here.

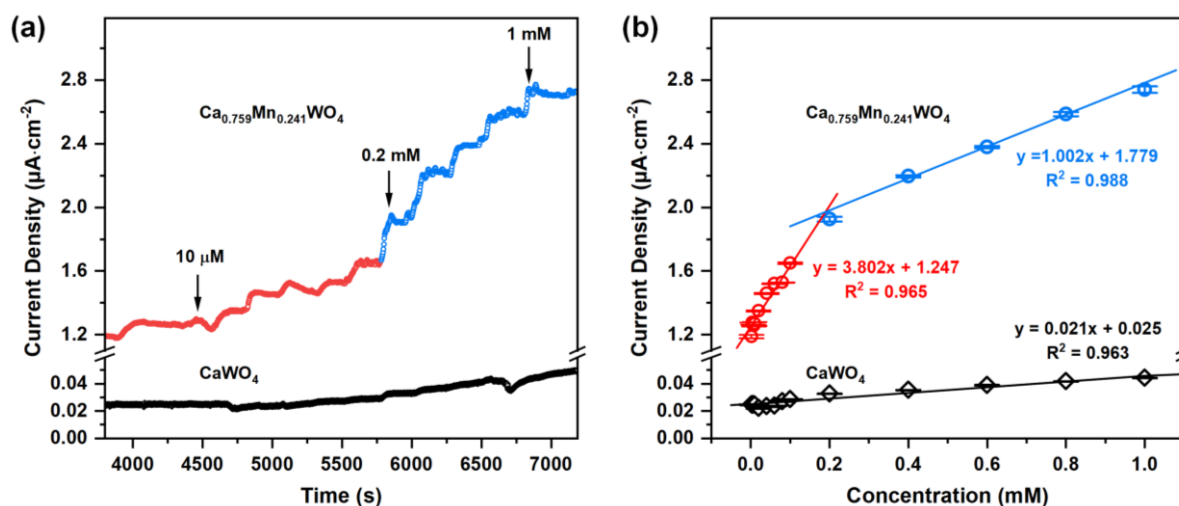


Figure 8. (a) Chronoamperometric glucose responses of $\text{Ca}_{0.759}\text{Mn}_{0.241}\text{WO}_4$ and CaWO_4 coated GCEs at 0.97 V vs. RHE in the glucose concentrations ranging from 0.002 to 1 mM. Corresponding glucose concentrations at three time points are marked to assist the interpretation of the plots. (b) Calibration curves for $\text{Ca}_{0.759}\text{Mn}_{0.241}\text{WO}_4$ and CaWO_4 coated

GCEs. The lower (0.002 to 0.2 mM) and higher (0.02 to 1 mM) glucose concentration ranges are highlighted in red and blue respectively in both (a) and (b). The curves are plotted based on the current density as a function of glucose concentration (CE: Pt, RE: Hg/HgO, 0.1 M NaOH, 3 s interval). The error bars in (b) represent the standard deviations calculated from three readings of current density after reaching after the addition of glucose stock solutions.

Detailed investigations are further carried out with $\text{Ca}_{0.759}\text{Mn}_{0.241}\text{WO}_4$ coated GCE since it triggers the strongest electrochemical response in glucose oxidations. Chronoamperometry at 0.97 V (vs. RHE) is performed for $\text{Ca}_{0.759}\text{Mn}_{0.241}\text{WO}_4$ and CaWO_4 coated GCEs, respectively, with step-wise additions of the glucose stock solutions, resulting in a gradual increase of the glucose concentration in the electrolyte solution from 0.002 to 1 mM (See Table S1 for the detailed protocol). The potential at 0.97 V (vs. RHE) is chosen because the electrochemical response is more stable at this region when compared with the current response in the region at around 1.5 V (vs. RHE) as demonstrated by the repeated CVs in Figure S10. Figure 8a shows a typical chronoamperometric response to a gradually increased glucose concentration for $\text{Ca}_{0.759}\text{Mn}_{0.241}\text{WO}_4$ coated GCE. Though CaWO_4 coated GCE also responds to the step-wise addition of glucose stock solutions, the increases in the current density are rather minimal.

The current density as a function of the glucose concentration is plotted based on the corresponding chronoamperometry as shown in Figure 8b. Two linear calibration curves are obtained for $\text{Ca}_{0.759}\text{Mn}_{0.241}\text{WO}_4$ coated GCE in the lower (0.002 to 0.2 mM) and higher (0.02 to 1 mM) glucose concentration ranges, respectively. This is most likely due to the electro-oxidation process becoming diffusion limited at higher glucose concentrations.⁶⁴ The linear regression equations reveal the corresponding sensitivities to be 3.80 and 1.00 $\mu\text{A}\cdot\text{mM}^{-1}\cdot\text{cm}^{-2}$ for the glucose concentration in the ranges of 0.002 – 0.2 and 0.2 – 1 mM, respectively. In comparison, the calibration curve for CaWO_4 coated GCE exhibits relatively poor linearity.

Admittedly, the absolute values of the sensitivities for $\text{Ca}_{0.759}\text{Mn}_{0.241}\text{WO}_4$ are far less impressive than those ($>1000 \mu\text{A}\cdot\text{mM}^{-1}\cdot\text{cm}^{-2}$) for the high-performing materials reported previously, such as NiCo_2O_4 nanoneedle-decorated electro-spun carbon nanofibers and Co_3O_4 ultra-nanosheet- $\text{Ni}(\text{OH})_2$.^{65,66} Nevertheless, incorporation of Mn in CaWO_4 at 24.1% lead to remarkable improvements of sensitivity by 237 and 60 times for both lower and higher concentration ranges, respectively, when compared to that ($0.021 \mu\text{A}\cdot\text{mM}^{-1}\cdot\text{cm}^{-2}$) of the almost non-active CaWO_4 (Figure 8b). Figure S11 shows the results of a preliminary investigation on the interference of cysteine, paracetamol, uric acid, and ascorbic acid during glucose oxidation at 0.97 V vs RHE. Both cysteine and paracetamol exhibit limited interference with a quick current recovery. Uric acid causes a significant current spike with relatively slow yet complete current recovery. Note that part of the current recovery occurs after the addition of paracetamol. Ascorbic acid demonstrates an extremely strong interfering effect with a huge current spike and very limited current recovery, which may be mitigated via strategies such as adjusting monitoring potential and/or introducing protective membrane in future studies.

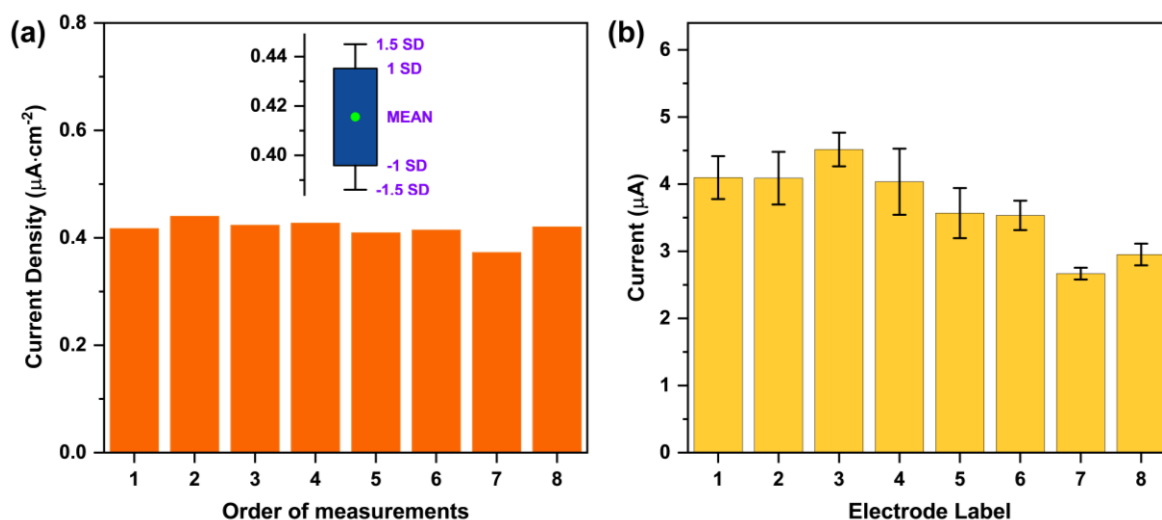


Figure 9. (a) Chronoamperometric response of $\text{Ca}_{0.759}\text{Mn}_{0.241}\text{WO}_4$ coated GCE at 0.97 V vs RHE in an electrolyte solution containing 0.1 mM glucose and 0.1 M NaOH. Inset: box plot visualising the mean and standard deviation of the dataset. (CE: Pt, RE: Hg/HgO). (b)

Assessment of reproducibility and repeatability: current readings of the measured CVs at 0.97 V vs. RHE for 8 replicates of $\text{Ca}_{0.759}\text{Mn}_{0.241}\text{WO}_4$ coated GCEs in an electrolyte solution containing 1 mM glucose and 0.1 M NaOH. Error bars show the standard deviation of 10 CV measurements for each electrode (CE: Pt, RE: Hg/HgO, 0.87 – 1.67 V vs. RHE, $50 \text{ mV}\cdot\text{s}^{-1}$).

The limit of detection (LOD) of $\text{Ca}_{0.759}\text{Mn}_{0.241}\text{WO}_4$ coated GCE is estimated using the method recommended in the literature via the following equation: $\text{LOD} = t_{\alpha, k-1} \cdot \sigma/m$, where Student's t -function $t_{0.02, 7}$ is set to 2.998 for 0.02-quantile (98% confidence level) at 7 ($k-1$) degrees of freedom, k , 8 in this study, is the number of measurements, σ is standard deviation of the measurements for electrolyte with low concentration glucose, and m is sensitivity determined from the calibration curve of the low concentration range.⁶⁷ σ is obtained by measuring the electrochemical response of a glucose solution with the concentration that is 1 – 5 times of the expected LOD.⁶⁷ Looking at the calibration curve of the lower concentration range in Figure 8b, we estimate that the LOD in the current study is in the range of 0.02 – 0.05 mM. Therefore, 0.1 mM (2 – 5 times of the expected LOD) glucose with the presence of 0.1 M NaOH is measured for 8 times to obtain the σ . Figure 9a shows the results of 8 measurements and the corresponding average current density with the standard deviation, from which the LOD is estimated to be $\sim 14 \mu\text{M}$.⁶⁸ The LOD obtained in this study is roughly in line with the range of LODs of Ni-, Co-, Cu-, and Mn-based oxides/hydroxides materials in the literature, albeit at the higher end.²⁴ Additionally, the lower limit of quantitation (LLOQ) is estimated to be $\sim 48 \mu\text{M}$ by the following equation: $\text{LLOQ} = 10 \cdot \sigma/m$,⁶⁸ where σ and m are defined the same as above for LOD.

The repeatability and reproducibility of $\text{Ca}_{0.759}\text{Mn}_{0.241}\text{WO}_4$ coated GCE are assessed by measuring 8 replicas of $\text{Ca}_{0.759}\text{Mn}_{0.241}\text{WO}_4$ coated GCE, each of which is subjected to 10 CV measurements in an electrolyte solution containing 1 mM glucose concentration and 0.1 M

NaOH as demonstrated in Figure 9b. The repeatability of $\text{Ca}_{0.759}\text{Mn}_{0.241}\text{WO}_4$ coated GCEs, established from the average relative standard deviation (RSD) between CV measurements, is calculated to be $\pm 8\%$ while the reproducibility, determined from the RSD between the currents of 8 electrodes, is found to be $\pm 17\%$. Though similar values were reported for a range of materials in the literature,^{69,70} the RSDs in this study are relatively high. This is most likely due to inconsistencies in the preparation of working electrodes and electrochemical measurements, which can be significantly improved by a future focused study on optimising and standardising the electrode preparation procedure and electrochemical measurement protocol.

Conclusion

This work reports on the controls over chemical compositions of mixed metal oxides via incorporating foreign metal ions (Mn^{2+}) in the crystal lattice of CaWO_4 nanocrystals and the resulting influences on the structural properties and the activity toward electrooxidation of glucose. $\text{Ca}_{1-x}\text{Mn}_x\text{WO}_4$ ($x = 0 - 0.241$) nanocrystals were successfully synthesised via a co-precipitation approach at 30 ± 2 °C, where $\text{Ca}_{1-x}\text{Mn}_x\text{WO}_4$ nanocrystals self-assembled into hierarchical sphere-like structures with the size ranging from submicron to a few microns. The presence of Mn in the precursors resulted in the partial deconstruction and shrinking of the sphere-like structures. Rietveld refinements revealed that the incorporation of Mn into CaWO_4 crystal lattice leads to isotropic contraction of the crystal cells with increasing Mn content, which further induced a slight blueshift of the bending mode of WO_4^{2-} at ~ 440 cm^{-1} and merging of the three rotation modes of WO_4^{2-} in the range between 360 to 260 cm^{-1} . Nonstoichiometric amorphous layer was found to exist on the surface of $\text{Ca}_{1-x}\text{Mn}_x\text{WO}_4$ nanocrystals with excessive Ca, Mn, and W. XPS analyses confirmed the presence of Mn^{3+} and W^{5+} , which are likely due to the need for compensating the charge imbalance caused by vacancies (particularly oxygen vacancies) and defects as commonly seen in materials

synthesised under mild temperatures. $\text{Ca}_{1-x}\text{Mn}_x\text{WO}_4$ is found to be active in electrooxidation of glucose, for which the activity is strongly related to the presence of Mn in CaWO_4 . The most active $\text{Ca}_{0.759}\text{Mn}_{0.241}\text{WO}_4$ demonstrated improvements in the activity by 237 and 60 times in terms of sensitivity for both lower (0.002 – 0.2 mM) and higher glucose concentration (0.2 – 1 mM) ranges, respectively, when compared to the nearly non-active CaWO_4 . The corresponding LOD and LLOQ were estimated to be 14 and 48 μM , respectively, with reasonable reproducibility and repeatability. The results in this study provide valuable information on further exploring the potentials of CaWO_4 as host materials in developing mixed metal oxides with multi-functionalities via a simple wet chemical co-precipitation approach.

ASSOCIATED CONTENT

Supporting Information. The Supporting Information is available free of charge at:

Further materials characterization data (PXRD, SEM, TEM, FT-IR, Rietveld Refinement data, estimated average crystal grain size, and additional electrochemical measurements data), experimental details for electrochemical measurements of chronoamperometry.

Funding Sources

European Union Horizon 2020 FlowPhotoChem project (Grant agreement number 862453); INTERREG Atlantic Area programme SEAFUEL project (Grant reference EAPA_190_2016); Taighde Éireann – Research Ireland under Grant number GOIPG/2021/1116; The Irish Government’s Programme for Research in Third Level Institutions, Cycles 4 and 5, National

Development Plan 2007–2013; MCIN/AEI/10.13039/501100011033 (Severo Ochoa CEX2021-001230-S).

Notes

The authors declare no competing financial interest.

ACKNOWLEDGMENT

This work received funding by European Union Horizon 2020 FlowPhotoChem project (Grant agreement number 862453), and was partially funded by INTERREG Atlantic Area programme SEAFUEL project (Grant reference EAPA_190_2016). LAN thanks the support from postgraduate scholarship by Taighde Éireann – Research Ireland under Grant number GOIPG/2021/1116. JA acknowledges financial support from the Spanish Ministry of Innovation and Science (Severo Ochoa CEX2021-001230-S funded by MCIN/AEI/10.13039/501100011033). LAN, HB, PF, and WT acknowledge the scientific and technical assistance of Dr. Éadaoin Timmins in the use of the SEM and TEM within the Centre for Microscopy & Imaging funded by University of Galway and the Irish Government's Programme for Research in Third Level Institutions, Cycles 4 and 5, National Development Plan 2007–2013.

References

- (1) Popov, N.; Bošković, M.; Perović, M.; Zadro, K.; Gilja, V.; Kratofil Krehula, L.; Robić, M.; Marciuš, M.; Ristić, M.; Musić, S.; Stanković, D.; Krehula, S. Effect of Ru³⁺ Ions on the Formation, Structural, Magnetic and Optical Properties of Hematite (α -Fe₂O₃) Nanorods. *J Magn Magn Mater* **2021**, *538*, 168316. <https://doi.org/10.1016/j.jmmm.2021.168316>.
- (2) Li, W.; Tong, W.; Etheridge, J.; Funston, A. M. Copper Assisted Symmetry and Size Control of Gold Nanobars. *J Mater Chem C Mater* **2023**, *11*, 5770–5778. <https://doi.org/10.1039/D2TC05286E>.

- (3) Gao, Y.; Cao, C.; Dai, L.; Luo, H.; Kanehira, M.; Ding, Y.; Wang, Z. L. Phase and Shape Controlled VO₂ Nanostructures by Antimony Doping. *Energy Environ Sci* **2012**, *5*, 8708–8715. <https://doi.org/10.1039/c2ee22290f>.
- (4) Li, W.; Tong, W.; Yadav, A.; Bladt, E.; Bals, S.; Funston, A. M.; Etheridge, J. Shape Control Beyond the Seeds in Gold Nanoparticles. *Chemistry of Materials* **2021**, *33*, 9152–9164. <https://doi.org/10.1021/acs.chemmater.1c02459>.
- (5) Zhang, Q.; Han, L.; Jing, H.; Blom, D. A.; Lin, Y.; Xin, H. L.; Wang, H. Facet Control of Gold Nanorods. *ACS Nano* **2016**, *10*, 2960–2974. <https://doi.org/10.1021/acsnano.6b00258>.
- (6) Hu, W.; Tong, W.; Li, L.; Zheng, J.; Li, G. Cation Non-Stoichiometry in Multi-Component Oxide Nanoparticles by Solution Chemistry: A Case Study on CaWO₄ for Tailored Structural Properties. *Physical Chemistry Chemical Physics* **2011**, *13*, 11634–11643. <https://doi.org/10.1039/c0cp02153a>.
- (7) Su, Y.; Li, L.; Li, G. Synthesis and Optimum Luminescence of CaWO₄-Based Red Phosphors with Codoping of Eu³⁺ and Na⁺. *Chemistry of Materials* **2008**, *20*, 6060–6067. <https://doi.org/10.1021/cm8014435>.
- (8) Van Embden, J.; Jasieniak, J.; Mulvaney, P. Mapping the Optical Properties of CdSe/CdS Heterostructure Nanocrystals: The Effects of Core Size and Shell Thickness. *J Am Chem Soc* **2009**, *131*, 14299–14309. <https://doi.org/10.1021/ja9030209>.
- (9) Wang, Y.; Li, L.; Li, G. Solvothermal Synthesis, Characterization and Photocatalytic Performance of Zn-Rich ZnWO₄ Nanocrystals. *Appl Surf Sci* **2017**, *393*, 159–167. <https://doi.org/10.1016/j.apsusc.2016.10.001>.
- (10) Tong, W.; Li, L.; Hu, W.; Yan, T.; Guan, X.; Li, G. Kinetic Control of MnWO₄ Nanoparticles for Tailored Structural Properties. *The Journal of Physical Chemistry C* **2010**, *114*, 15298–15305. <https://doi.org/10.1021/jp103879c>.
- (11) Diéguez, A.; Romano-Rodríguez, A.; Vilà, A.; Morante, J. R. The Complete Raman Spectrum of Nanometric SnO₂ Particles. *J Appl Phys* **2001**, *90*, 1550–1557. <https://doi.org/10.1063/1.1385573>.
- (12) Zhang, L.; Liu, J.; Xiao, H.; Liu, D.; Qin, Y.; Wu, H.; Li, H.; Du, N.; Hou, W. Preparation and Properties of Mixed Metal Oxides Based Layered Double Hydroxide as Anode Materials for Dye-Sensitized Solar Cell. *Chemical Engineering Journal* **2014**, *250*, 1–5. <https://doi.org/10.1016/j.cej.2014.03.098>.
- (13) Wang, L.; Chen, L.; Liu, M.; Liu, J.; Xiao, S.; Bi, F.; Zhao, L.; Li, Y. Hierarchical MnCo₂O₄@MnWO₄ Core-Shell Nanoarrays on Ni Foam as Binder-Free Electrode for Asymmetric Supercapacitors. *Electrochim Acta* **2024**, *507*, 145135. <https://doi.org/10.1016/j.electacta.2024.145135>.
- (14) Samira, S.; Hong, J.; Camayang, J. C. A.; Sun, K.; Hoffman, A. S.; Bare, S. R.; Nikolla, E. Dynamic Surface Reconstruction Unifies the Electrocatalytic Oxygen Evolution Performance of Nonstoichiometric Mixed Metal Oxides. *JACS Au* **2021**, *1*, 2224–2241. <https://doi.org/10.1021/jacsau.1c00359>.

- (15) Wang, H.; Zhang, H.; Zhao, K.; Nie, A.; Alharthi, S.; Amin, M. A.; El-Bahy, Z. M.; Li, H.; Chen, L.; Xu, B. Bin; Ma, Y.; Li, T. Research Progress on Electromagnetic Wave Absorption Based on Magnetic Metal Oxides and Their Composites. *Adv Compos Hybrid Mater* **2023**, *6*, 120. <https://doi.org/10.1007/s42114-023-00694-5>.
- (16) Han, Z.; Zhang, S.; Yan, G.; Yi, S.; Wang, Y.; Hou, X.; Zhang, Z.; Zhang, L. A Colorimetric Sensor Array Consisted of $\text{Ca}_x\text{Mn}_{1-x}\text{WO}_4$ with High Oxidase-like Activity to Detect Antioxidants. *Sens Actuators B Chem* **2025**, *422*, 136620. <https://doi.org/10.1016/j.snb.2024.136620>.
- (17) Cao, B.; Liu, Q.; Qiu, L.; Weng, Y.; He, Y.; Han, X.; Dong, B. Unveiling the Subtle Emission Transition of Dysprosium in CaWO_4 Crystals for Ultra-Sensitive Ratiometric Thermometry and Anti-Counterfeiting Applications. *Ceram Int* **2025**, *51*, 40683–40691. <https://doi.org/10.1016/j.ceramint.2025.06.306>.
- (18) Liu, S.-L.; Liu, B.; Xiang, Z.; Xu, L.; Wang, X.-F.; Liu, Y.; Wang, X. Fabrication of CaWO_4 Microspheres with Enhanced Sonocatalytic Performance for Ciprofloxacin Removal in Aqueous Solution. *Colloids Surf A Physicochem Eng Asp* **2021**, *628*, 127206. <https://doi.org/10.1016/j.colsurfa.2021.127206>.
- (19) Su, Y.; Li, L.; Li, G. Self-Assembly and Multicolor Emission of Core/Shell Structured $\text{CaWO}_4:\text{Na}^+/\text{Ln}^{3+}$ Spheres. *Chemical Communications* **2008**, 4004–4006. <https://doi.org/10.1039/b810648g>.
- (20) Kolesnikov, I. E.; Mamonova, D. V.; Kurochkin, M. A.; Medvedev, V. A.; Kolesnikov, E. Yu. Multimode Optical Thermometry Using CaWO_4 Emission Band. *J Alloys Compd* **2024**, *1007*, 176466. <https://doi.org/10.1016/j.jallcom.2024.176466>.
- (21) Bilgin Simsek, E.; Tuna, Ö. Understanding the Nature of Ce–Fe Synergy in The Structure CaWO_4 Scheelite for Enhanced Photocatalytic Performance Under Visible Light. *Ceram Int* **2024**, *50*, 20600–20611. <https://doi.org/10.1016/j.ceramint.2024.03.181>.
- (22) Wu, H.; Peng, J.; Sun, H.; Ruan, Q.; Dong, H.; Jin, Y.; Sun, Z.; Hu, Y. Surface Activation of Calcium Tungstate by Europium Doping for Improving Photocatalytic Performance: Towards Lanthanide Site Photocatalysis. *Chemical Engineering Journal* **2022**, *432*, 134339. <https://doi.org/10.1016/j.cej.2021.134339>.
- (23) Yang, H.; Hu, Y.; Yin, X.; Huang, J.; Qiao, C.; Hu, Z.; He, C.; Huo, D.; Hou, C. A Disposable and Sensitive Non-Enzymatic Glucose Sensor Based on a 3D-Mn-Doped NiO Nanoflower-Modified Flexible Electrode. *Analyst* **2023**, *148*, 153–162. <https://doi.org/10.1039/D2AN01495E>.
- (24) Hwang, D.-W.; Lee, S.; Seo, M.; Chung, T. D. Recent Advances in Electrochemical Non-Enzymatic Glucose Sensors – A Review. *Anal Chim Acta* **2018**, *1033*, 1–34. <https://doi.org/10.1016/j.aca.2018.05.051>.
- (25) Gomez, A. M.; Lopez, J. C. Bringing Color to Sugars: The Chemical Assembly of Carbohydrates to BODIPY Dyes. *The Chemical Record* **2021**, *21*, 3112–3130. <https://doi.org/10.1002/tcr.202100190>.

- (26) Kurniawan, F.; Tsakova, V.; Mirsky, V. M. Gold Nanoparticles in Nonenzymatic Electrochemical Detection of Sugars. *Electroanalysis* **2006**, *18*, 1937–1942. <https://doi.org/10.1002/elan.200603607>.
- (27) Naikoo, G. A.; Awan, T.; Salim, H.; Arshad, F.; Hassan, I. U.; Pedram, M. Z.; Ahmed, W.; Faruck, H. L.; Aljabali, A. A. A.; Mishra, V.; Serrano-Aroca, Á.; Goyal, R.; Negi, P.; Birkett, M.; Nasef, M. M.; Charbe, N. B.; Bakshi, H. A.; Tambuwala, M. M. Fourth-generation Glucose Sensors Composed of Copper Nanostructures for Diabetes Management: A Critical Review. *Bioeng Transl Med* **2022**, *7*, e10248. <https://doi.org/10.1002/btm2.10248>.
- (28) Nemati, S. S.; Dehghan, G.; Rashtbari, S.; Tan, T. N.; Khataee, A. Enzyme-Based and Enzyme-Free Metal-Based Glucose Biosensors: Classification and Recent Advances. *Microchemical Journal* **2023**, *193*, 109038. <https://doi.org/10.1016/j.microc.2023.109038>.
- (29) Jasrotia, R.; Raj, K.; Singh, B.; Alluhayb, A. H.; Younis, A. M.; Suman; Ramya, M.; Kandwal, A.; Khanna, V.; Singh, V. P.; Kit, C. C. Innovative Ferrite Sensors: Advancing Non-Enzymatic Glucose Detection. *Sensors and Actuators Reports* **2025**, *9*, 100295. <https://doi.org/10.1016/j.snr.2025.100295>.
- (30) Zhu, H.; Li, L.; Zhou, W.; Shao, Z.; Chen, X. Advances in Non-Enzymatic Glucose Sensors Based on Metal Oxides. *J Mater Chem B* **2016**, *4*, 7333–7349. <https://doi.org/10.1039/C6TB02037B>.
- (31) Filimonenkov, I. S.; Mokhova, A. I.; Urvanov, S. A.; Kurzhumbaev, D. Zh.; Batova, N. I.; Skryleva, E. A. α -MnO₂ with a Cryptomelane Structure for the Non-Enzymatic Glucose Electrooxidation in a Neutral Medium. *Electrochim Acta* **2024**, *508*, 145267. <https://doi.org/10.1016/j.electacta.2024.145267>.
- (32) Gao, J.; Meng, T.; Lu, S.; Ma, X.; Zhang, Y.; Fu, D.; Lu, Z.; Li, C. M. Manganese-Doped Tremella-like Nickel Oxide as Biomimetic Sensors toward Highly Sensitive Detection of Glucose in Human Serum. *Journal of Electroanalytical Chemistry* **2020**, *863*, 114071. <https://doi.org/10.1016/j.jelechem.2020.114071>.
- (33) Patterson, A. L. The Scherrer Formula for X-Ray Particle Size Determination. *Physical Review* **1939**, *56*, 978–982. <https://doi.org/10.1103/PhysRev.56.978>.
- (34) Marinakis, K. I.; Kelsall, G. H. Adsorption of Dodecyl Sulfate and Decyl Phosphonate on Wolframite, (Fe, Mn)WO₄, and Their Use in the Two-Liquid Flotation of Fine Wolframite Particles. *J Colloid Interface Sci* **1985**, *106*, 517–531. [https://doi.org/10.1016/S0021-9797\(85\)80027-8](https://doi.org/10.1016/S0021-9797(85)80027-8).
- (35) Liu, X.; Xiao, C. Wolframite Solubility and Precipitation in Hydrothermal Fluids: Insight from Thermodynamic Modeling. *Ore Geol Rev* **2020**, *117*, 103289. <https://doi.org/10.1016/j.oregeorev.2019.103289>.
- (36) Blanchard, F. N. X-Ray Powder Data for CaWO₄, Synthetic Scheelite. *Powder Diffraction* **1989**, *4*, 220–222. <https://doi.org/10.1017/S0885715600013774>.

- (37) Shannon, R. D. Revised Effective Ionic Radii and Systematic Studies of Interatomic Distances in Halides and Chalcogenides. *Acta Crystallographica Section A* **1976**, *32*, 751–767. <https://doi.org/10.1107/S0567739476001551>.
- (38) Rietveld, H. M. A Profile Refinement Method for Nuclear and Magnetic Structures. *J Appl Crystallogr* **1969**, *2*, 65–71. <https://doi.org/10.1107/S0021889869006558>.
- (39) Toby, B. H.; Von Dreele, R. B. *GSAS-II*: The Genesis of a Modern Open-Source All Purpose Crystallography Software Package. *J Appl Crystallogr* **2013**, *46*, 544–549. <https://doi.org/10.1107/S0021889813003531>.
- (40) MURAI, K.; YAMASHITA, K.; KITAHARA, G.; TOKUDA, M.; YOSHIASA, A. Syntheses, Single Crystal Structure Analyses and Ultraviolet Light Emission of $\text{CaW}_{1-x}\text{Mo}_x\text{O}_4$ ($x = 0.0\text{--}1.0$) Scheelite-Powellite Solid Solutions. *Journal of Mineralogical and Petrological Sciences* **2023**, *118*, 220901. <https://doi.org/10.2465/jmps.220901>.
- (41) Toby, B. H. *R* Factors in Rietveld Analysis: How Good Is Good Enough? *Powder Diffr* **2006**, *21*, 67–70. <https://doi.org/10.1154/1.2179804>.
- (42) Vegard, L. Die Konstitution Der Mischkristalle Und Die Raumfüllung Der Atome. *Zeitschrift für Physik* **1921**, *5*, 17–26. <https://doi.org/10.1007/BF01349680>.
- (43) Su, Y.; Li, G.; Xue, Y.; Li, L. Tunable Physical Properties of CaWO_4 Nanocrystals via Particle Size Control. *The Journal of Physical Chemistry C* **2007**, *111*, 6684–6689. <https://doi.org/10.1021/jp068480p>.
- (44) Tong, W.; Li, L.; Hu, W.; Yan, T.; Li, G. Systematic Control of Monoclinic CdWO_4 Nanophase for Optimum Photocatalytic Activity. *The Journal of Physical Chemistry C* **2010**, *114*, 1512–1519. <https://doi.org/10.1021/jp910284u>.
- (45) Maheshwary; Singh, B. P.; Singh, R. A. Color Tuning in Thermally Stable Sm^{3+} -Activated CaWO_4 Nanophosphors. *New Journal of Chemistry* **2015**, *39*, 4494–4507. <https://doi.org/10.1039/C4NJ01911C>.
- (46) Katrib, A.; Hemming, F.; Wehrer, P.; Hilaire, L.; Maire, G. The Multi-Surface Structure and Catalytic Properties of Partially Reduced WO_3 , WO_2 and $\text{WC} + \text{O}_2$ or $\text{W} + \text{O}_2$ as Characterized by XPS. *J Electron Spectros Relat Phenomena* **1995**, *76*, 195–200. [https://doi.org/10.1016/0368-2048\(95\)02451-4](https://doi.org/10.1016/0368-2048(95)02451-4).
- (47) Ryu, J. H.; Yoon, J.-W.; Shim, K. B.; Sasaki, T.; Koshizaki, N. Room-Temperature Deposition of Nanocrystalline CaWO_4 Films by Pulsed Laser and Their Optical Properties. *J Appl Phys* **2006**, *99*, 086103. <https://doi.org/10.1063/1.2186370>.
- (48) Guo, C.; Yin, S.; Yan, M.; Kobayashi, M.; Kakihana, M.; Sato, T. Morphology-Controlled Synthesis of $\text{W}_{18}\text{O}_{49}$ Nanostructures and Their Near-Infrared Absorption Properties. *Inorg Chem* **2012**, *51*, 4763–4771. <https://doi.org/10.1021/ic300049j>.
- (49) Peng, S.; Chen, Z.; Wang, J.; Yu, M.; Niu, X.; Cui, T.; Ao, R.; Cai, H.; Huang, H.; Lin, L.; Chen, X.; Yang, H. One-Pot Synthesis of Oxygen Vacancy-Rich Amorphous/Crystalline Heterophase CaWO_4 Nanoparticles for Enhanced

- Radiodynamic-Immunotherapy. *Advanced Science* **2025**, *12*, 2409551.
<https://doi.org/10.1002/advs.202409551>.
- (50) Frankcombe, T. J.; Liu, Y. Interpretation of Oxygen 1s X-Ray Photoelectron Spectroscopy of ZnO. *Chemistry of Materials* **2023**, *35*, 5468–5474.
<https://doi.org/10.1021/acs.chemmater.3c00801>.
- (51) Goddard, W. A. Surface Science. In *Computational Materials, Chemistry, and Biochemistry: From Bold Initiatives to the Last Mile*; Shankar, S., Muller, R., Dunning, T., Chen, G. H., Eds.; Springer, Cham, 2021; Vol. 284, pp 1119–1125.
https://doi.org/10.1007/978-3-030-18778-1_51.
- (52) Junta-Rosso, J. L.; Hochella, M. F. The Chemistry of Hematite 001 Surfaces. *Geochim Cosmochim Acta* **1996**, *60*, 305–314. [https://doi.org/10.1016/0016-7037\(95\)00382-7](https://doi.org/10.1016/0016-7037(95)00382-7).
- (53) Li, F.; Ruan, S.; Yin, Y.; Zhang, N.; Zhang, H.; Li, C.; Chen, Y. Facile Synthesis of MnWO₄/WO₃ Electrospun Nanofibers as High Performance Visible-Light Driven Photocatalysts. *Mater Lett* **2018**, *229*, 98–102.
<https://doi.org/10.1016/j.matlet.2018.06.118>.
- (54) Zaidi, S. Z. A.; Orton, B. . R.; Beynon, J. X-Ray Photoelectron Spectroscopy of Co-Evaporated Mn/SiO_x Thin Films. *Physica Status Solidi (a)* **1996**, *159*, K1–K4.
- (55) Barker Jr., A. S. Infrared Lattice Vibrations in Calcium Tungstate and Calcium Molybdate. *Physical Review* **1964**, *135*, A742–A747.
<https://doi.org/10.1103/PhysRev.135.A742>.
- (56) Porto, S. P. S.; Scott, J. F. Raman Spectra of CaWO₄, SrWO₄, CaMoO₄, and SrMoO₄. *Physical Review* **1967**, *157*, 716–719. <https://doi.org/10.1103/PhysRev.157.716>.
- (57) Russell, J. P.; Loudon, R. The First-Order Raman Spectrum of Calcium Tungstate. *Proceedings of the Physical Society* **1965**, *85*, 1029–1033.
<https://doi.org/10.1088/0370-1328/85/5/321>.
- (58) Abozaid, R. M.; Lazarevic, Z. Ž.; Radojevic, V.; Rabasovic, M. S.; Sevic, D. D.; Rabasovic, M.; Romcevic, N. Z. Characterization of Neodymium Doped Calcium Tungstate Single Crystal by Raman, IR and Luminescence Spectroscopy. *Science of Sintering* **2018**, *50*, 445–455. <https://doi.org/10.2298/SOS1804445A>.
- (59) Yin, Y.; Li, Y.-N.; Liu, S.; Jiang, Y.; Liu, X.-Y.; Zhang, P. Theoretical Study of Efficient Photon–Phonon Resonance Absorption in the Tungsten-Related Vibrational Mode of Scheelite. *ACS Omega* **2024**, *9*, 10517–10521.
<https://doi.org/10.1021/acsomega.3c08636>.
- (60) Abozaid, R. M.; Lazarević, Z. Ž.; Tomić, N.; Milutinović, A.; Šević, D.; Rabasović, M. S.; Radojević, V. Optical Properties CaWO₄:Nd³⁺/PMMA Composite Layered Structures. *Opt Mater* **2019**, *96*, 109361.
<https://doi.org/10.1016/j.optmat.2019.109361>.
- (61) Guo, M. Q.; Hong, H. S.; Tang, X. N.; Fang, H. D.; Xu, X. H. Ultrasonic Electrodeposition of Platinum Nanoflowers and Their Application in Nonenzymatic

- Glucose Sensors. *Electrochim Acta* **2012**, *63*, 1–8.
<https://doi.org/10.1016/j.electacta.2011.11.114>.
- (62) Dai, W.; Wu, B.; Zhang, F.; Huang, Y.; Zhao, C.; Zhang, Y.; Cui, C.; Guo, J.; Huang, S. Construction of Bimetallic Oxy-Hydroxides Based on Ni(OH)₂ Nanosheets for Sensitive Non-Enzymatic Glucose Detection *via* Electrochemical Oxidation and Incorporation. *Nanoscale* **2025**, *17*, 2589–2598.
<https://doi.org/10.1039/D4NR04342A>.
- (63) Qi, C.; Zhang, C.; Yang, Z. Engineering Co₃O₄ with Co Defects for Highly Sensitive Nonenzymatic Detection of Glucose. *Colloids Surf A Physicochem Eng Asp* **2022**, *654*, 130096. <https://doi.org/10.1016/j.colsurfa.2022.130096>.
- (64) Liu, K.; Duan, X.; Yuan, M.; Xu, Y.; Gao, T.; Li, Q.; Zhang, X.; Huang, M.; Wang, J. How to Fit a Response Current-Concentration Curve? A Semi-Empirical Investigation of Non-Enzymatic Glucose Sensor based on PANI-Modified Nickel Foam. *Journal of Electroanalytical Chemistry* **2019**, *840*, 384–390.
<https://doi.org/10.1016/j.jelechem.2019.04.018>.
- (65) Liu, L.; Wang, Z.; Yang, J.; Liu, G.; Li, J.; Guo, L.; Chen, S.; Guo, Q. NiCo₂O₄ Nanoneedle-Decorated Electrospun Carbon Nanofiber Nanohybrids for Sensitive Non-Enzymatic Glucose Sensors. *Sens Actuators B Chem* **2018**, *258*, 920–928.
<https://doi.org/10.1016/j.snb.2017.11.118>.
- (66) Mahmoudian, M. R.; Basirun, W. J.; Woi, P. M.; Sookhakian, M.; Yousefi, R.; Ghadimi, H.; Alias, Y. Synthesis and Characterization of Co₃O₄ Ultra-Nanosheets and Co₃O₄ Ultra-Nanosheet-Ni(OH)₂ as Non-Enzymatic Electrochemical Sensors for Glucose Detection. *Materials Science and Engineering: C* **2016**, *59*, 500–508.
<https://doi.org/10.1016/j.msec.2015.10.055>.
- (67) Loock, H.-P.; Wentzell, P. D. Detection Limits of Chemical Sensors: Applications and Misapplications. *Sens Actuators B Chem* **2012**, *173*, 157–163.
<https://doi.org/10.1016/j.snb.2012.06.071>.
- (68) Daniel C. Harris. *Quantitative Chemical Analysis*, 7th ed.; W.H. Freeman and Company: New York, 2007.
- (69) Yang, J.; Yu, J.-H.; Rudi Strickler, J.; Chang, W.-J.; Gunasekaran, S. Nickel Nanoparticle–Chitosan-Reduced Graphene Oxide-Modified Screen-Printed Electrodes for Enzyme-Free Glucose Sensing in Portable Microfluidic Devices. *Biosens Bioelectron* **2013**, *47*, 530–538. <https://doi.org/10.1016/j.bios.2013.03.051>.
- (70) Cherevko, S.; Chung, C.-H. The Porous CuO Electrode Fabricated by Hydrogen Bubble Evolution and Its Application to Highly Sensitive Non-Enzymatic Glucose Detection. *Talanta* **2010**, *80*, 1371–1377. <https://doi.org/10.1016/j.talanta.2009.09.038>.